

The Effect of Black-Dot Defects on FeCrAl Radiation Hardening

Jian Sun ¹, Miaosen Yu ¹, Zhixian Wei ¹, Hui Dai ¹ , Wenxue Ma ¹, Yibin Dong ¹ , Yong Liu ^{1,*}, Ning Gao ^{1,2} 
and Xuelin Wang ^{1,*} 

¹ Institute of Frontier and Interdisciplinary Science and Key Laboratory of Particle Physics and Particle Irradiation (MOE), Shandong University, Qingdao 266237, China

² Institute of Modern Physics, Chinese Academy of Sciences, Lanzhou 730000, China

* Correspondence: 202090900041@sdu.edu.cn (Y.L.); xuelinwang@sdu.edu.cn (X.W.)

Abstract: FeCrAl is regarded as one of the most promising cladding materials for accident-tolerant fuel at nuclear fission reactors due to its comprehensive properties of inherent corrosion resistance, excellent irradiation resistance, high-temperature oxidation resistance, and stress corrosion cracking resistance. In this work, the irradiation response of FeCrAl irradiated by 2.4 MeV He²⁺ ions with a fluence of $1.1 \times 10^{16} \text{ cm}^{-2}$ at room temperature was studied using X-ray diffraction, transmission electron microscopy, and nanoindentation. The characterization results of structural and mechanical properties showed that only black-dot defects exist in irradiated FeCrAl samples, and that the hardness of the irradiated samples was 11.5% higher than that of the unirradiated samples. Similar to other types of radiation defects, black-dot defects acted as fixed defect obstacles and hindered the movement of slip dislocations moving under the applied load, resulting in a significant increase in the hardness of FeCrAl. Importantly, this work points out that irradiation-induced black-dot defects can significantly affect the mechanical properties of materials, and that their contribution to radiation hardening cannot be ignored.

Keywords: FeCrAl; ion irradiation; black-dot defects; irradiation hardening



Citation: Sun, J.; Yu, M.; Wei, Z.; Dai, H.; Ma, W.; Dong, Y.; Liu, Y.; Gao, N.; Wang, X. The Effect of Black-Dot Defects on FeCrAl Radiation Hardening. *Metals* **2023**, *13*, 458. <https://doi.org/10.3390/met13030458>

Academic Editor: Ilana Perelshtein

Received: 4 January 2023

Revised: 14 February 2023

Accepted: 20 February 2023

Published: 22 February 2023



Copyright: © 2023 by the authors. Licensee MDPI, Basel, Switzerland. This article is an open access article distributed under the terms and conditions of the Creative Commons Attribution (CC BY) license (<https://creativecommons.org/licenses/by/4.0/>).

1. Introduction

The continuous development of nuclear energy is inseparable from many basic research fields, such as nuclear waste treatment and advanced nuclear energy material research [1–3], and promotes the development of energy, materials, and other fields. Since the 2011 Fukushima nuclear accident in Japan, the industry attaches great importance to the development of a new generation of accident-tolerant fuel (ATF) cladding materials that improve the ability of cladding to resist high-temperature accidents [4–6]. As one of the most promising cladding materials for ATF technology for light water reactors, FeCrAl alloys have impressive mechanical properties and high temperature corrosion resistance compared with traditional zirconium alloys due to the formation of a protective film of aluminum oxide, thereby fundamentally eliminating the con-zirconium water reaction [7–10]. However, it has been found that irradiation hardening could occur under a high-energy flux circumstance [11,12], which limits the service life for the nuclear reactor in commission.

Unlike γ -ray irradiation [13,14], high-energy ion irradiation results in the material's lattice atoms being knocked out of their initial positions by incident particles and then interacting with the surrounding matrix to generate a collision cascade. During the quenching period of the collision cascade, a number of point defects, including interstitials and vacancies, recombine; the accumulation of the remaining point defects leads to the formation of defect clusters, such as dislocation loops and voids [15], and even causes phase transition in irradiated material [16]. These defects (dislocation loops in particular) could lead to irradiation hardening and the embrittlement of structural materials, which are obstacles for gliding dislocation [17,18]. In bcc iron and iron-based alloys, the natural Burger vectors of dislocation loops have either $\langle 100 \rangle$ or $1/2\langle 111 \rangle$. To date, the fast one-dimensional

diffusion of $1/2\langle 111 \rangle$ dislocation loops allows itself to be absorbed by other sinks, such as other dislocation loops, precipitates, and grain boundaries, whereas $\langle 100 \rangle$ loops with a sessile nature are almost immobile and accumulate in the microstructure once formed, making them a stationary sink for mobile point defects [19–23]. According to the experiment conducted by Yao et. al., dislocation loops with the characteristics of $1/2\langle 111 \rangle$ and $\langle 100 \rangle$ exist in pure iron at room temperature [19]. Under high-dose radiation conditions, dislocation loops with the characteristic of $1/2\langle 111 \rangle$ are dominant in irradiation production [21]. The addition of chromium content improves the strength of obstacles hindering the gliding of dislocation due to the increment of unpinning stress, which was studied by Yao et.al [20]. Computationally, Cr segregation during the dislocation enhances its ability to impede the motion of the dislocation line, thereby further inducing the degradation of structural material [24]. The enrichment of Cr inhibits the motion of glissile dislocation loops and the subsequent coalescence between dislocation loops, resulting in increased dislocation density.

Thus far, many experimental results show that FeCrAl alloys and FeCr alloys exhibit similar structural and mechanical responses under irradiation. Currently, investigations regarding the radiation hardening of FeCrAl are generally conducted experimentally and computationally. A variety of in situ TEM experiments under Kr^{++} ion irradiation at 320 °C for a series of FeCrAl alloys with Cr content of 10~18 wt% and Al content of 3~5 wt% conducted by Haley et al. showed that a larger proportion of dislocation loops with the characteristic of $1/2\langle 111 \rangle$ exist in irradiated materials [25]. It was proposed that the content of $1/2\langle 111 \rangle$ dislocation loops increased with increasing Al content. Additionally, the simulation work conducted by Yu et al. showed that Al could be segregated to dislocation loops with $1/2\langle 111 \rangle$ and $\langle 100 \rangle$ characteristics, and further improve the obstacle strength with relatively lower content [26]. It was thus found that the evolution behavior of dislocation loops and Cr-rich phases could be regulated by changing the Cr and Al contents. However, there has been relatively few studies regarding helium irradiation of FeCrAl alloys, and these have mainly focused on the evolution behavior of helium bubbles. He ion irradiation usually induces the formation of black-dot defects, dislocation loops, and He bubbles in FeCrAl [15,27], which accelerates the degradation of FeCrAl properties. Prokhodtseva's and Schäuble et al.'s studies showed that implanted He atoms inhibit the generation of $\langle 100 \rangle$ dislocation loops by blocking the movement of $1/2\langle 111 \rangle$ dislocation loops [28]. Previous studies have shown that a material's elemental composition, irradiation-induced defect clusters, material phase transitions, and dislocation loops can significantly affect material hardness [29–31]. However, the formation of black-dot defects induced by irradiation is often accompanied by the appearance of dislocation loops and sedimentary facies. Given the small size of black-dot defects, their effect on radiation hardening has often been ignored; it is difficult to identify whether black-dot defects significantly contribute to radiation hardening. Therefore, it is important to independently study the influence of black-dot defects induced by irradiation on the hardness of FeCrAl, which is conducive to the evaluation of FeCrAl irradiation hardening.

In this work, a Fe-10Cr-4Al sample was irradiated by 2.4 MeV He^{2+} ions with a fluence of $1.1 \times 10^{16} \text{ cm}^{-2}$ at room temperature in order to investigate the effect of black-dot defects induced by ions irradiation on the hardness of FeCrAl. Based on X-ray diffraction (XRD), transmission electron microscope (TEM) microstructure characterization, and nanoindentation analysis, the microstructure and corresponding hardness evolution of FeCrAl were investigated after ion irradiation.

2. Materials and Methods

The material used in this study was FeCrAl alloy (Fe-10Cr-4Al) with body-centered-cubic (bcc) structure; the weight percent (wt%) of Fe, Cr, and Al elements were 86 wt%, 10 wt%, and 4 wt%, respectively. The pure Fe (99.50 wt%), pure Cr (99.00 wt%), and pure Al (99.60 wt%) were first melted in a 25 kg vacuum induction furnace into an ingot [32] using a magnesia crucible; the vacuum degree was less than 100 Pa. The ingot was then

homogenized at 1150 °C for 3 h, hot rolled at 800 °C, and annealed at 1000 °C for 1 h. Subsequently, the ingot was cut into several 13 × 13 × 5 mm pieces, which were electrolytically polished. Samples were irradiated by 2.4 MeV He²⁺ ions with a fluence of 1.1 × 10¹⁶ cm⁻² at room temperature utilizing the Low Energy intense-highly-charged ion Accelerator Facility (LEAF) at the Institute of Modern Physics, Chinese Academy of Sciences. To avoid undesired heating of the FeCrAl samples, a relatively low beam flux (5.456 × 10¹¹ cm⁻² s⁻¹) was constantly maintained during the entire irradiation process; thus, the self-annealing phenomenon during irradiation that can heal induced lattice damage could be considered negligible. As shown in Figure 1, the depth profiles of displacements per atom (dpa) and He concentration were determined through the Stopping and Range of Ions in Matter (SRIM) 2013 quick simulation code [33,34] with 40 eV displacement threshold energy for elements Fe, Cr, and Al. The maximum damage and irradiation were located around depths of 4.02 μm and 4.08 μm from the irradiated surface, corresponding to dpa and He concentration of 0.6 and 0.5%, respectively. In addition, both decreased to zero at a depth of 4.38 μm after reaching the corresponding peak.

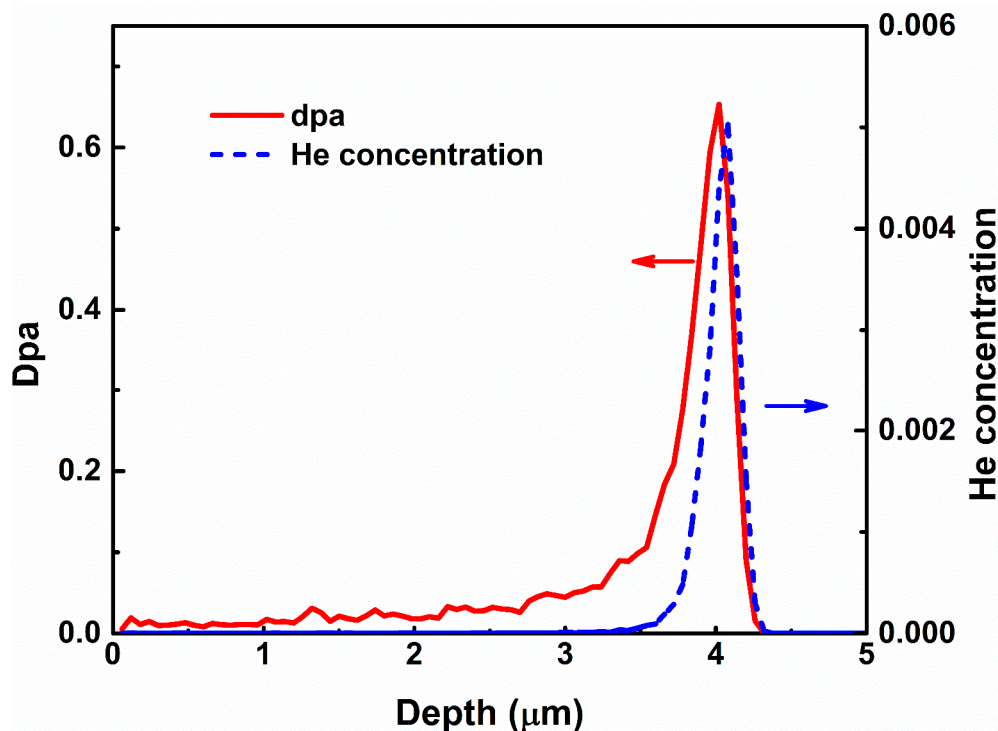


Figure 1. Distributions of dpa and He concentration as a function of penetration depth for 2.4 MeV He²⁺ ions in FeCrAl based on SRIM 2013 simulation.

The XRD experiments were performed on the polished surface (irradiated surface) of the samples using a Bruker D8 Advance diffractometer equipped with a copper anticathode; the diffraction patterns were recorded between 40° and 85° in 2θ scale with a step size of 0.02°. The penetration depth was approximately 6 μm and covered the entire irradiation region [35]. A cross-sectional TEM sample was prepared using an ion milling process performed using a focused ion beam mill, in addition to a lift-out process performed using an FEI Helios NanoLab 600 Dual Beam system. TEM images were obtained using an FEI Tecnai G2 F20 transmission electron microscope. Quantitative analysis for the number density of black-dot defects was conducted using images acquired at the different selected regions with the thickness of the corresponding area obtained by convergent beam electron diffraction (CBED) patterns [36]. Notably, the TEM experiment time for each sample was quite short, and electron beam irradiation did not generate noticeable annealing and recrystallization of lattice damage. To determine hardness, nanoindentation tests

utilizing an Agilent Nano Indenter G200 (Agilent Technologies, Inc., Santa Clara, CA, USA) were performed on the polished surface (irradiated surface) of FeCrAl. The continuous stiffness measurement (CSM) was performed using a Berkovich diamond indenter tip with a diameter of 20 μm . Using a continuous measure of contact stiffness during loading, hardness as a continuous function of depth from a single indentation test was obtained. The maximum depth of all indentation tests was set to 3 μm , and 10 indentation tests were made in each sample to obtain an average value.

3. Results and Discussion

3.1. Irradiation-Induced Structural Evolution

The XRD patterns obtained from virgin and irradiated FeCrAl samples are shown in Figure 2. As evidence, FeCrAl samples exhibited three characteristic peaks at $2\theta = 44.5^\circ$, 64.5° , and 81.7° , as shown in Figure 2a, corresponding to reflections from the (110), (200), and (211) planes (PDF#54-1410), respectively. Compared with the virgin FeCrAl sample, no new peaks appeared in the XRD pattern of the irradiated FeCrAl sample, indicating that no observable phase transition occurred. In order to accurately determine the peak evolution induced by ion irradiation, the (211) planes of the virgin and He irradiated samples were finely scanned. As shown in Figure 2b, compared with the peak position and full width at half maximum of the virgin, the finely scanned results confirmed that the XRD peak position of the irradiated sample has no shift and no observable change in the broadening, further indicating that the crystal structure was stable, and the irradiated regions of the samples remained in the original phase under 2.4 MeV He^{2+} irradiation with a fluence of $1.1 \times 10^{16} \text{ cm}^{-2}$ at room temperature. Therefore, changes in the microstructure and nanohardness were primarily caused by the formation and evolution of defects induced by ion irradiation rather than by phase transitions or precipitation.

TEM observations were performed on sample cross-sections to visually characterize and confirm the structural damage evolution induced by 2.4 MeV He^{2+} ion irradiation. A low magnification cross-sectional dark-field TEM image shows that He^{2+} ion irradiation led to a region of damage with a thickness of $\sim 600 \text{ nm}$ below 3600 nm on the sample surface, as shown in Figure 3a. No nanoprecipitates were observed, which was consistent with the XRD characterization results. The SRIM-simulated dpa profile is also displayed in Figure 3a for comparison with the TEM result, and indicates that the damaged region corresponds to a dpa value range of 0.14–0.65. Furthermore, compared with the region near the surface (Figure 3b) without observable defects, the TEM image of the damaged region (Figure 3c) shows that distinct punctate defects (black-dot defects) dominated the damaged microstructure, which appeared as white dots under dark-field conditions. In addition, adjusting the focal length of the objective lens to overfocus and underfocus during the TEM observation process did not find any obvious features of observed helium bubbles, ruling out the possibility that these dot defects were He bubbles. Figure 3d,e are the dark-field and bright-field TEM images of the damaged peak region, respectively. Several small-sized black-dot defects ($<1 \text{ nm}$) could not be clearly counted. Therefore, only the number density of larger size ($>1 \text{ nm}$) black-dot defects was calculated, which was $\sim 9.22 \times 10^{23} \text{ m}^{-3}$. The TEM observation results confirmed that the irradiation conditions of 2.4 MeV He ion irradiation with a fluence of $1.1 \times 10^{16} \text{ cm}^{-2}$ at room temperature did not induce the formation of deposition phases or He bubbles in the FeCrAl used in this study; however, it did induce a large number of black-dot defects in the region near the damage peak.

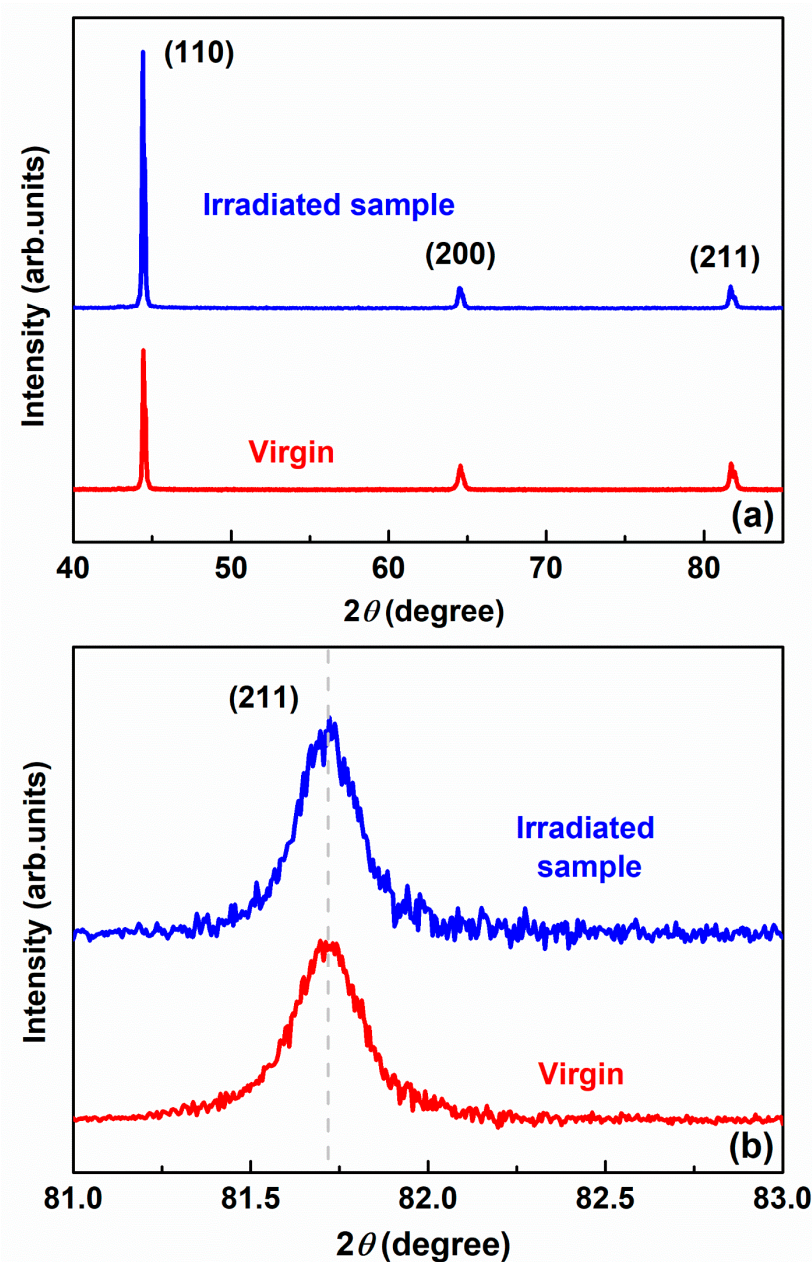


Figure 2. (a) XRD patterns and (b) finely scanned XRD patterns around (211) peak of virgin and irradiated FeCrAl samples.

3.2. Irradiation-Induced Hardness Evolution

In order to characterize the effect of black-dot defects on the hardness of FeCrAl, nanoindentation tests with CSM were performed on virgin and irradiated FeCrAl samples. The depth profiles of the averaged nanoindentation hardness of virgin and irradiated samples are shown in Figure 4a; all hardness averages continuously decreased with increasing indent depth due to the indentation size effect (ISE) [37]. The measured hardness at indentation depths less than 80 nm was ignored due to uncertainty caused by surface artifacts and the indenter tip complexity [22,38]. In addition, the radius of the plastically affected zone was usually several times the indentation depth during nanoindentation testing. Therefore, the unirradiated regions started to affect the hardness data (the softer substrate effect (SSE)) when the indentation depth exceeded a certain value. As shown in Figure 4b, the ratio of the average hardness values of the irradiated sample (H_{irr}) and the virgin sample (H_{vir}) at the indentation depth peaked with the increase in indentation

depth at approximately 900 nm. Beyond the depth of peak (900 nm), the SSE started to influence the accuracy of the measurement of hardness in the irradiated region, and caused a decrease in relative hardening [39]. It is worth noting that the peak depth (900 nm) was approximately 1/4.5 of the depth (4080 nm) of the irradiation damage layer, which indicates that for the FeCrAl used in our work, the indenter reflected the hardness of the indentation region, and extended down nearly 4.5 times the contact depth.

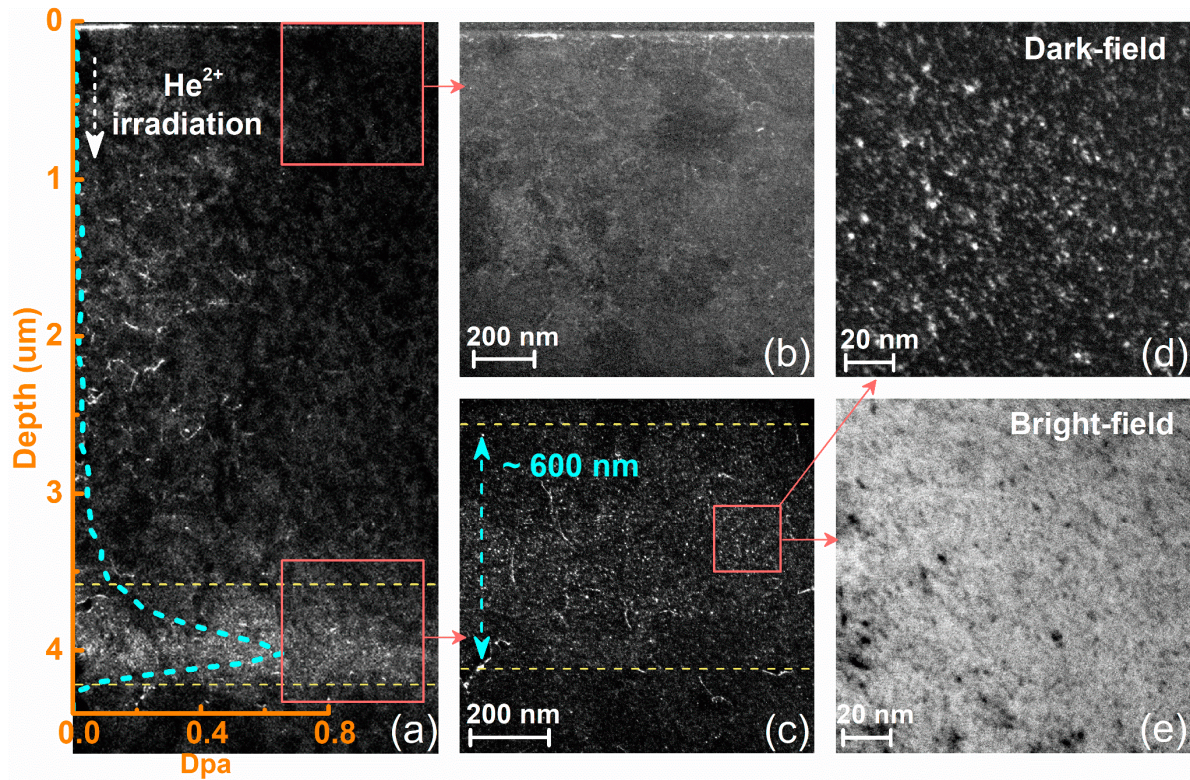


Figure 3. Dark-field cross-section TEM images of (a) the entire irradiation region, (b) the surface region, (c,d) damaged peak regions, and (e) the bright-field cross-section TEM image of the damaged peak region.

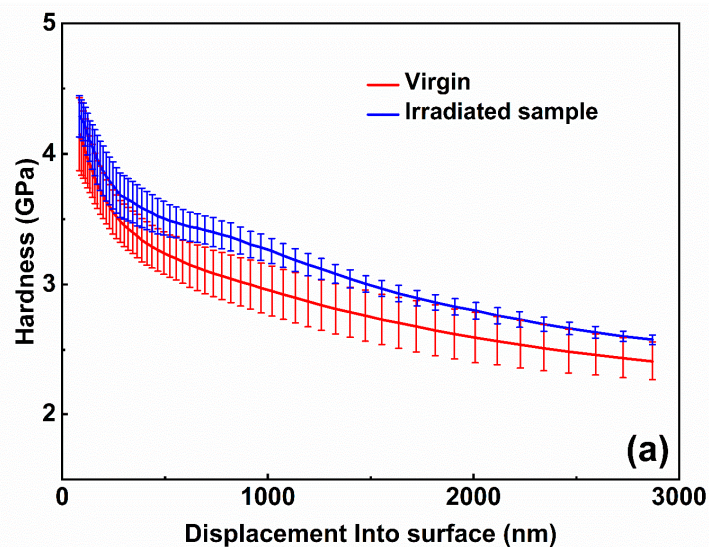


Figure 4. Cont.

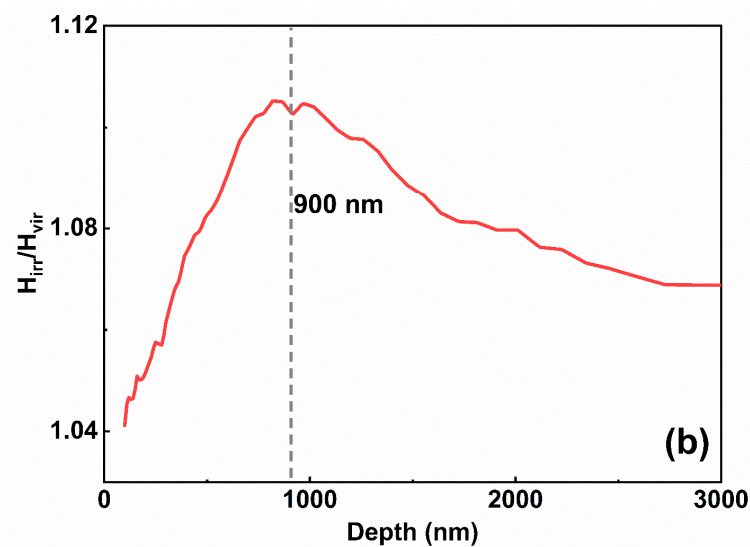


Figure 4. (a) Relationships between the hardness and indentation depths of the virgin and irradiated samples, and (b) dependence of the ratio of H_{irr}/H_{vir} on indentation depth.

The Nix–Gao model, based on the geometrical necessary dislocation (GND) [40], was utilized to eliminate the ISE and obtain an accurate hardness independent of the indentation depth. The model’s description of the relationship between hardness and indentation depth is as follows:

$$H = H_0 \sqrt{1 + \frac{h^*}{h}} \quad (1)$$

where H is the measured hardness, h is the indentation depth, H_0 is the hardness in the limit of infinite depth, and h^* is a characteristic length that depends on the indenter and the specific material. Despite the damage gradient effect (DGE), the Nix–Gao model is extensively used to evaluate the bulk equivalent hardness of thin ion-irradiated layers [41–44].

Figure 5a shows the profiles plots of H^2 versus h^{-1} , which reveal that the profile of the irradiated sample exhibited bilinearity. The inflection point was located at a depth of ~ 900 nm, which was consistent with the depth corresponding to the position of the ratio peak in Figure 4b. However, the curve of the unirradiated sample also showed a slight bilinearity due to significant surface effects. Therefore, assuming that the surface effect had the same effect for irradiated and unirradiated samples, the amount of H_0 of samples in the range of 80–900 nm was calculated using the Nix–Gao model to minimize the surface effect on hardening irradiation measurement. As shown in Figure 5b, compared with the 2.87 GPa hardness of the unirradiated sample, the hardness of the irradiated sample increased to 3.20 GPa, which was approximately 11.5% higher than the unirradiated sample. The increase in hardness of irradiated samples indicates that irradiation-induced black-dot defects could significantly affect the mechanical properties of materials. Irradiation-induced black-dot defects were typically sessile, as opposed to glissile dislocations, which might have moved under an externally applied load. In addition, further irradiation led to Cr segregation on these defects, allowing defects to become more stable in bulk and to grow further [24]. Due to Cr segregation, black-dot defects became stronger obstacles compared with non-decorated defects. As a result, the possible Cr segregation at irradiation-induced black-dot defects contributed to hardening. Therefore, the interaction of dislocations with black-dot defects can be interpreted as the collision of several gliding dislocations with fixed defect obstructions, which ultimately results in radiation hardening.

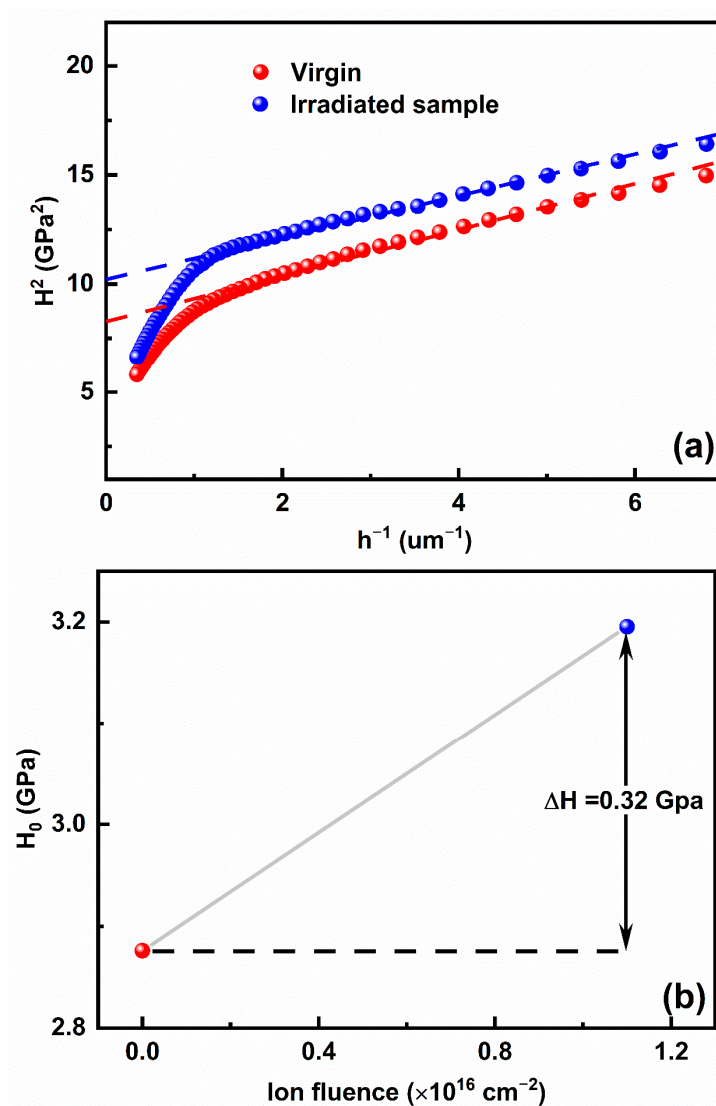


Figure 5. (a) The profile plots of H^2 versus h^{-1} for virgin and irradiated samples, and (b) hardness variation in FeCrAl induced by He ion irradiation.

4. Conclusions

In this study, the effect of black-dot defects on the hardness of FeCrAl subjected to He^{2+} irradiation at room temperature was investigated based on the characterization of structural and mechanical properties. The structural characterization results show that He ion irradiation did not induce the formation of He bubbles or new phases in FeCrAl, but did induce many black-dot defects at the end of the irradiating region. The black-dot defects could act as fixed obstacles and hindered the movement of slip dislocations under the applied load, thereby affecting the hardness of FeCrAl. Compared with the 2.87 GPa hardness of the unirradiated sample, the hardness of the irradiated sample increased to 3.20 GPa, an increase of 11.5%. This study confirmed that, consistent with the effect of dislocation loops, the small black-dot defects induced by irradiation could significantly affect the hardness of FeCrAl.

Author Contributions: Conceptualization, Y.L. and N.G.; methodology, Y.L. and X.W.; validation, J.S. and M.Y.; formal analysis, J.S., M.Y., Z.W., H.D., W.M., Y.D. and Y.L.; investigation, J.S., M.Y., Z.W., H.D. and Y.L.; resources, Y.L.; data curation, Y.L., N.G. and X.W.; writing—original draft preparation, J.S. and Y.L.; writing—review and editing, J.S., M.Y., Z.W. and Y.L.; visualization, J.S. and Y.L.; funding acquisition, Y.L. and X.W. All authors have read and agreed to the published version of the manuscript.

Funding: This work was supported by the National Natural Science Foundation of China (grant numbers 12105159 and 12175125); the Natural Science Foundation of Shandong Province of China (grant number ZR2021QA102); and a China Postdoctoral Science Foundation funded project (grant number 2021M691915).

Data Availability Statement: Data is available upon request from the corresponding authors.

Acknowledgments: This work was supported by the Low Energy intense-highly-charged ion Accelerator Facility (LEAF) at the Institute of Modern Physics, Chinese Academy of Sciences.

Conflicts of Interest: The authors declare no conflict of interest.

References

1. Awual, M.R.; Suzuki, S.; Taguchi, T.; Shiwaku, H.; Okamoto, Y.; Yaita, T. Radioactive cesium removal from nuclear wastewater by novel inorganic and conjugate adsorbents. *Chem. Eng. J.* **2014**, *242*, 127–135. [[CrossRef](#)]
2. Shen, N.; Yang, Z.; Liu, S.; Dai, X.; Xiao, C.; Taylor-Pashow, K.; Li, D.; Yang, C.; Li, J.; Zhang, Y.; et al. $^{99}\text{TcO}_4^-$ removal from legacy defense nuclear waste by an alkaline-stable 2D cationic metal organic framework. *Nat. Commun.* **2020**, *11*, 5571. [[CrossRef](#)] [[PubMed](#)]
3. Was, G.S.; Petti, D.; Ukai, S.; Zinkle, S. Materials for future nuclear energy systems. *J. Nucl. Mater.* **2019**, *527*, 151837. [[CrossRef](#)]
4. Terrani, K.A.; Zinkle, S.J.; Snead, L.L. Advanced oxidation-resistant iron-based alloys for LWR fuel cladding. *J. Nucl. Mater.* **2014**, *448*, 420–435. [[CrossRef](#)]
5. Hellstrom, K.; Hall, J.; Malmberg, P.; Cao, Y.; Norell, M.; Svensson, J.E. Mitigation of fireside corrosion in power plants: The combined effect of sulfur dioxide and potassium chloride on the corrosion of a FeCrAl alloy. *Energy Fuels* **2014**, *28*, 6116–6129. [[CrossRef](#)]
6. Zinkle, S.J.; Terrani, K.A.; Snead, L.L. Motivation for utilizing new high-performance advanced materials in nuclear energy systems. *Curr. Opin. Solid State Mater. Sci.* **2016**, *20*, 401–410. [[CrossRef](#)]
7. Cheng, T.; Keiser, J.R.; Brady, M.P.; Terrani, K.A.; Pint, B.A. Oxidation of fuel cladding candidate materials in steam environments at high temperature and pressure. *J. Nucl. Mater.* **2012**, *427*, 396–400. [[CrossRef](#)]
8. Pint, B.A.; Terrani, K.A.; Brady, M.P.; Cheng, T.; Keiser, J.R. High temperature oxidation of fuel cladding candidate materials in steam–hydrogen environments. *J. Nucl. Mater.* **2013**, *440*, 420–427. [[CrossRef](#)]
9. Ott, L.J.; Robb, K.R.; Wang, D. Preliminary assessment of accident-tolerant fuels on LWR performance during normal operation and under DB and BDB accident conditions. *J. Nucl. Mater.* **2014**, *448*, 520–533. [[CrossRef](#)]
10. Lim, J.; Hwang, I.S.; Kim, J.H. Design of alumina forming FeCrAl steels for lead or lead–bismuth cooled fast reactors. *J. Nucl. Mater.* **2013**, *441*, 650–660. [[CrossRef](#)]
11. Porollo, S.I.; Dvoriashin, A.M.; Vorobyev, A.N.; Konobeev, Y.V. The microstructure and tensile properties of Fe–Cr alloys after neutron irradiation at 400 C to 5.5–7.1 dpa. *J. Nucl. Mater.* **1998**, *256*, 247–253. [[CrossRef](#)]
12. Field, K.G.; Briggs, S.A.; Sridharan, K.; Howard, R.H.; Yamamoto, Y. Mechanical properties of neutron-irradiated model and commercial FeCrAl alloys. *J. Nucl. Mater.* **2017**, *489*, 118–128. [[CrossRef](#)]
13. Rashad, M.; Saudi, H.A.; Zakaly, H.M.; Issa, S.A.; Abd-Elnaiem, A.M. Control optical characterizations of Ta⁺⁵-doped B₂O₃–Si₂O–CaO–BaO glasses by irradiation dose. *Opt. Mater.* **2021**, *112*, 110613. [[CrossRef](#)]
14. Mohamed, M.; Moustafa, S.; Abd-Elnaiem, A.M.; Abdel-Rahim, M.A. The optical parameters of γ -irradiated and annealed thin films of Ge₁₅Se₅₀Te₃₅. *J. Alloys Compd.* **2015**, *647*, 771–777. [[CrossRef](#)]
15. Mansur, L.K. Theory and experimental background on dimensional changes in irradiated alloys. *J. Nucl. Mater.* **1994**, *216*, 97–123. [[CrossRef](#)]
16. Deng, T.; Sun, J.; Tai, P.; Wang, Y.; Zhang, L.; Chang, H.; Wang, Z.; Niu, L.; Sheng, Y.; Xue, D.; et al. Ti₃AlC₂, a candidate structural material for innovative nuclear energy system: The microstructure phase transformation and defect evolution induced by energetic heavy-ion irradiation. *Acta Mater.* **2020**, *189*, 188–203. [[CrossRef](#)]
17. Zinkle, S.J.; Matsukawa, Y. Observation and analysis of defect cluster production and interactions with dislocations. *J. Nucl. Mater.* **2004**, *329*, 88–96. [[CrossRef](#)]
18. Han, X.; Zhang, C.; Niu, M.; Ding, Z.; Jang, J.; Wang, T.; Kimura, A. A comparison study of change in hardness and microstructures of a Zr-added FeCrAl ODS steel irradiated with heavy ions. *Mater. Sci. Eng. A* **2022**, *841*, 143050. [[CrossRef](#)]
19. Yao, Z.; Jenkins, M.L.; Hernández-Mayoral, M.; Kirk, M.A. The temperature dependence of heavy-ion damage in iron: A microstructural transition at elevated temperatures. *Philos. Mag.* **2010**, *90*, 4623–4634. [[CrossRef](#)]
20. Yao, Z.; Hernández-Mayoral, M.; Jenkins, M.L.; Kirk, M.A. Heavy-ion irradiations of Fe and Fe–Cr model alloys Part 1: Damage evolution in thin-foils at lower doses. *Philos. Mag.* **2008**, *88*, 2851–2880. [[CrossRef](#)]
21. Hernández-Mayoral, M.; Yao, Z.; Jenkins, M.L.; Kirk, M.A. Heavy-ion irradiations of Fe and Fe–Cr model alloys Part 2: Damage evolution in thin-foils at higher doses. *Philos. Mag.* **2008**, *88*, 2881–2897. [[CrossRef](#)]
22. Schäublin, R.; Décamps, B.; Prokhodtseva, A.; Löffler, J.F. On the origin of the primary $\frac{1}{2}$ a₀ and a₀ loops in irradiated Fe(Cr) alloys. *Acta Mater.* **2017**, *133*, 427–439. [[CrossRef](#)]

23. Chen, W.Y.; Miao, Y.; Gan, J.; Okuniewski, M.A.; Maloy, S.A.; Stubbins, J.F. Neutron irradiation effects in Fe and Fe-Cr at 300 °C. *Acta Mater.* **2016**, *111*, 407–416. [[CrossRef](#)]
24. Terentyev, D.; Bakaev, A. Radiation-induced strengthening and absorption of dislocation loops in ferritic Fe-Cr alloys: The role of Cr segregation. *J. Phys. Condens. Matter* **2013**, *25*, 265702. [[CrossRef](#)] [[PubMed](#)]
25. Haley, J.C.; Briggs, S.A.; Edmondson, P.D.; Sridharan, K.; Roberts, S.G.; Lozano-Perez, S.; Field, K.G. Dislocation loop evolution during in-situ ion irradiation of model FeCrAl alloys. *Acta Mater.* **2017**, *136*, 390–401. [[CrossRef](#)]
26. Yu, M.; Wang, Z.; Wang, F.; Setyawan, W.; Long, X.; Liu, Y.; Dong, L.; Gao, N.; Gao, F.; Wang, X. Coupled effect of Cr and Al on interactions between a prismatic interstitial dislocation loop and an edge dislocation line in Fe-Cr-Al alloy. *Acta Mater.* **2023**, *245*, 118651. [[CrossRef](#)]
27. Chen, Y.; Li, Y.; Ran, G.; Wu, L.; Ye, C.; Han, Q.; Wang, H.; Du, H. In-situ TEM observation of the evolution of dislocation loops and helium bubbles in a pre helium irradiated FeCrAl alloy during annealing. *Prog. Nucl. Energy* **2020**, *129*, 103502. [[CrossRef](#)]
28. Prokhodtseva, A.; Décamps, B.; Ramar, A.; Schäublin, R. Impact of He and Cr on defect accumulation in ion-irradiated ultrahigh-purity Fe (Cr) alloys. *Acta Mater.* **2013**, *61*, 6958–6971. [[CrossRef](#)]
29. Li, F.; Long, Y.; Guo, D.; Guo, L.; Lin, W.; Chen, Y.; Li, L.; Ren, Q.; Liao, Y. Ion Irradiation Defects and Hardening in FeCrAl Alloy. *Metals* **2022**, *12*, 1645. [[CrossRef](#)]
30. Kondo, K.; Aoki, S.; Yamashita, S.; Ukai, S.; Sakamoto, K.; Hirai, M.; Kimura, A. Ion irradiation effects on FeCrAl-ODS ferritic steel. *Nucl. Mater. Energy* **2018**, *15*, 13–16. [[CrossRef](#)]
31. Aydogan, E.; Weaver, J.S.; Maloy, S.A.; El-Atwani, O.; Wang, Y.Q.; Mara, N.A. Microstructure and mechanical properties of FeCrAl alloys under heavy ion irradiations. *J. Nucl. Mater.* **2018**, *503*, 250–262. [[CrossRef](#)]
32. Wang, P.; Qiao, Y.; Qi, W.; Du, S.; Liu, Z.; Meng, F.; Zhang, X.; Wang, K.; Li, Q.; Yao, Z.; et al. Preparation and Properties Study of Cr on FeCrAl Cladding Materials. *Front. Mater.* **2021**, *8*, 621086. [[CrossRef](#)]
33. Ziegler, J.F.; Ziegler, M.D.; Biersack, J.P. SRIM—The stopping and range of ions in matter (2010). *Nucl. Instrum. Methods Phys. Res. Sect. B* **2010**, *268*, 1818–1823. [[CrossRef](#)]
34. Stoller, R.E.; Toloczko, M.B.; Was, G.S.; Certain, A.G.; Dwaraknath, S.; Garner, F.A. On the use of SRIM for computing radiation damage exposure. *Nucl. Instrum. Methods Phys. Res. Sect. B* **2013**, *310*, 75–80. [[CrossRef](#)]
35. Wang, Y.; Zhou, W.; Wen, Q.; Ruan, X.; Luo, F.; Bai, G.; Qing, Y.; Zhu, D.; Huang, Z.; Zhang, Y.; et al. Behavior of plasma sprayed Cr coatings and FeCrAl coatings on Zr fuel cladding under loss-of-coolant accident conditions. *Surf. Coat. Technol.* **2018**, *344*, 141–148. [[CrossRef](#)]
36. Allen, S.M.; Hall, E.L. Foil thickness measurements from convergent-beam diffraction patterns an experimental assessment of errors. *Philos. Mag. A* **1982**, *46*, 243–253. [[CrossRef](#)]
37. Pharr, G.M.; Herbert, E.G.; Gao, Y. The indentation size effect: A critical examination of experimental observations and mechanistic interpretations. *Annu. Rev. Mater. Res.* **2010**, *40*, 271–292. [[CrossRef](#)]
38. Kwon, J.; Kwon, S.C.; Hong, J.H. Prediction of radiation hardening in reactor pressure vessel steel based on a theoretical model. *Ann. Nucl. Energy* **2003**, *30*, 1549–1559. [[CrossRef](#)]
39. Li, S.; Wang, Y.; Dai, X.; Liu, F.; Li, J.; Wang, X. Evaluation of hardening behaviors in ion-irradiated Fe–9Cr and Fe–20Cr alloys by nanoindentation technique. *J. Nucl. Mater.* **2016**, *478*, 50–55. [[CrossRef](#)]
40. Nix, W.D.; Gao, H. Indentation size effects in crystalline materials: A law for strain gradient plasticity. *J. Mech. Phys. Solids* **1998**, *46*, 411–425. [[CrossRef](#)]
41. Hosemann, P.; Kiener, D.; Wang, Y.; Maloy, S.A. Issues to consider using nano indentation on shallow ion beam irradiated materials. *J. Nucl. Mater.* **2012**, *425*, 136–139. [[CrossRef](#)]
42. Kasada, R.; Takayama, Y.; Yabuuchi, K.; Kimura, A. A new approach to evaluate irradiation hardening of ion-irradiated ferritic alloys by nano-indentation techniques. *Fusion Eng. Des.* **2011**, *86*, 2658–2661. [[CrossRef](#)]
43. Miyazawa, T.; Nagasaka, T.; Kasada, R.; Hishinuma, Y.; Muroga, T.; Watanabe, H.; Yamamoto, T.; Nogami, S.; Hatakeyama, M. Evaluation of irradiation hardening of ion-irradiated V–4Cr–4Ti and V–4Cr–4Ti–0.15 Y alloys by nanoindentation techniques. *J. Nucl. Mater.* **2014**, *455*, 440–444. [[CrossRef](#)]
44. Kareer, A.; Prasitthipayong, A.; Krumwiede, D.; Collins, D.M.; Hosemann, P.; Roberts, S.G. An analytical method to extract irradiation hardening from nanoindentation hardness-depth curves. *J. Nucl. Mater.* **2018**, *498*, 274–281. [[CrossRef](#)]

Disclaimer/Publisher’s Note: The statements, opinions and data contained in all publications are solely those of the individual author(s) and contributor(s) and not of MDPI and/or the editor(s). MDPI and/or the editor(s) disclaim responsibility for any injury to people or property resulting from any ideas, methods, instructions or products referred to in the content.